Comparing the growth kinetics of cell populations in two and three dimensions

M. Radszuweit,[1,*] M. Block,[1,†] J. G. Hengstler,[2] E. Schöll,[1,‡] and D. Drasdo[3,§]
[1]*Institut für Theoretische Physik, Technische Universität Berlin, D-10623 Berlin, Germany*
[2]*Institut für Arbeitsphysiologie, Universität Dortmund, D-44139 Dortmund, Germany*
[3]*French National Institute for Computer Science and Control, Rocquencourt, B.P. 105, 8153 Le Chesnay Cedex, France and Interdisciplinary Center for Bioinformatics, University of Leipzig, D-04107 Leipzig, Germany*
(Received 13 February 2009; published 12 May 2009)

We study the kinetics of growing cell populations by means of a kinetic Monte Carlo method. By applying the same growth mechanism to a two-dimensional (2D) and a three-dimensional (3D) model, and making direct comparison with experimental studies, we show that both models exhibit similar behavior. Based on this we propose a method for establishment of a mapping between the 2D and 3D results. Additionally, we present an analytic approach to obtain the time evolution, and show in case of the 3D model how synchronization effects can influence the growth kinetics. Finally, we compare the results of our models to experimental data of the growth kinetics of 2D monolayers and 3D NIH3T3 xenografts in mice.

DOI: 10.1103/PhysRevE.79.051907 PACS number(s): 87.18.Hf

I. INTRODUCTION

The study of cell population growth and in particular of tumor growth by modeling the basic interactions has attracted wide interest. Both reaction-diffusion-type or continuum mechanical models, where densities of cells are considered (for reviews, see [1–5]), and individual-cell-based models, where the basic modeling unit is the individual cell (for reviews, see [6–10]), have been considered to analyze aspects of tumor growth on different spatial scales.

By systematic investigation of the influence of different mechanisms in such models which determine the behavior of individual cells, one can understand how mechanisms on the cell scale affect the macroscopic growth kinetics of a tumor. On the other hand, models of molecular regulation built into each individual cell within an individual-cell-based model allow one to understand how molecular changes affect cell behavior. Linking both can permit prediction of the impact of molecular changes on the growth dynamics of tumors [11–13]. Previous theoretical studies have established that both the growth kinetics and surface dynamics of cell lines growing as two-dimensional (2D) monolayers *in vitro* can be modeled by a two-dimensional cellular automaton [14]. These results can be seen in direct comparison with the experimental investigation of tumor cell monolayers studied by Brú *et al.* [15]. Detailed experiments with different cell lines *in vitro* and *in vivo* result in universal critical surface dynamics, which characterizes these types of mainly malignant tumor cells [15–18]. It has recently been shown that this critical surface dynamics corresponds to the Kardar-Parisi-Zhang (KPZ) universality class [14], in contrast to earlier interpretations by Brú *et al.* [15].

It remains as largely open question in how far predictions from the 2D investigation can be mapped directly to three-dimensional (3D) investigations. If so, 2D models could constitute a very useful tool to draw conclusions also about 3D cell populations. In this paper we study the relationship between the 2D model and a corresponding 3D model, both based on individual cells as the elementary modeling unit. We show in detail the coincidence of the basic properties. Additionally we propose a 3D mean-field model which opens up the possibility to map the results from the single-cell-based model in three dimensions, where computational expense becomes a problem, to a simplified 3D model at considerably reduced computational effort. This becomes crucial if growth and therapy of tumors at the stage of clinical manifestation should be modeled because at this stage the tumors are usually of centimeter size, and thus have $\sim 10^9$–10^{10} cells. Such population sizes are not amenable to individual-cell-based models. We compare our models to experimental findings on (*in vitro*) monolayers (two dimensions) and (*in vivo*) NIH3T3 mouse-fibroblast xenografts grown in mice (three dimensions).

Synchronization effects in cell populations play an important role in clinical research (see, e.g., [19–21]). The effects of synchronization on the growth kinetics of tumor cells have been known for a long time (see, e.g., [22]). It has been shown that the degree of synchronization can significantly affect the growth speed of tumors [23]. So it is an important question to know how long these colonies stay synchronized, since certain tumor therapy approaches are based on most cells being in the same stage in cell cycle (see, e.g., [24–28]). In the framework of our model we are able to give an answer to that question.

II. MODELING

For both models, in two and in three dimensions, some basic rules have to be fulfilled. The models should be based on individual cell actions. By comparison with experimental data of monolayers and xenografts (tumors that emerge from the injection of tumor cells into animals), we find that it is sufficient to include only basic aspects of cell behavior to explain the data and reproduce some more general features

*radszuweit@itp.physik.tu-berlin.de
†Present address: Bayer Technology Services GmbH.
‡FAX: +49-(0)30-314-21130; schoell@itp.physik.tu-berlin.de
§dirk.drasdo@inria.fr

of solid tumors. We here consider cell division and migration controlled by contact inhibition of cell division and contact inhibition of cell migration. The lack of nutrients as a growth-limiting factor was not taken into account since in the growth data we compared our simulation results to, nutrients were not limiting. Necrosis and apoptosis were neglected for the same reason. However, the effect of apoptosis on the growth kinetics within our models can be considered over a wide range of apoptosis rates by a rescaling of growth rate.

The 3D model, as explained later, will be modified to permit simulations of large cell populations up to the centimeter-sized tumors. Here a kind of mean field is used to reduce the computational expense. First, we introduce the individual-cell-based model. We describe the model in detail in case of two dimensions, and further elaborate the specific differences to the 3D case.

A. Two-dimensional model

1. Lattice

To avoid lattice artifacts in our results we use Voronoi cells [29] to construct a lattice that is unstructured but has a well-defined distribution of the cell area. Our construction is divided into the following steps.

We take a simple square lattice of size $L=l\times l$ points with a lattice constant a. All cells here then have a cell area $A=a^2$, where the overall area is $[(l-1)a]^2$ (noting that a lattice with l points has $l-1$ divisions).

The second step is to distribute points randomly in every square. We insert exactly one point into each square, which leads to $(l-1)\times(l-1)$ construction points for our Voronoi diagram. According to the Voronoi property, all those points in space are assigned to a construction point such that they are closer to that construction point than to any other construction point. The dual graph of a Voronoi diagram is the Delaunay diagram. It connects all those construction points in space that are neighbors in the Voronoi diagram [30].

The lattice resulting from this algorithm has the following properties:

(a) $(l-1)\times(l-1)$ points with a well-defined neighborhood of on average six neighbors as a result of the Delaunay triangulation;

(b) a predescribed average cell area of $\bar{A}=a^2$ with a well-defined sharply peaked distribution around the average (determined by the choice of one point in each square); and

(c) a well-defined correspondence of the lattice points to the cell structure on the dual graph.

2. Rules

As basic processes within our cell population growth model, we consider division and migration of cells. Apoptosis, which for moderate rates only rescales the growth rate, and mutations can be easily added (see [14,31]) but are neglected in this paper. The lattice structure in our model does not determine anything about the structure of the cell, so cell division is reduced to modeling the cell-cycle time and its distribution. The cell cycle consists of distinct phases, namely, the mitosis phase (M phase), the DNA duplication phase (S phase), and gap phases, in which cell signaling and individual cell conditions determine the time. The cell cycle is controlled by cell-cycle checkpoints [32]. For the total duration of the cell cycle, experiments indicate a Γ-like distribution, which is why we here model the cell-cycle time τ using the discrete analog to the Γ distribution, the Erlang distribution in Eq. (1),

$$f(\tau')=\lambda_m\frac{(\lambda_m\tau')^{m-1}}{(m-1)!}\exp\{-\lambda_m\tau'\}. \tag{1}$$

Here $\lambda_m=m$ such that $\langle\tau'\rangle\equiv\bar{\tau}=1$. The parameter m controls the shape of the cell-cycle time distribution. As can be easily seen from the equation, $m=1$ corresponds to a Poisson distribution. For $m\to\infty$ the distribution converges against a δ distribution, implying that the cell-cycle time is the same for all cells. For values between $m\approx 5$ and $m\approx 60$ the shape of the cell-cycle time distribution resembles well that found in experiments with radioactive thymidine as a cell proliferation marker (e.g., [33]).

In our model cell division is the same as the occupation of a new lattice point. We describe the biological process of one mother cell dividing into two daughter cells by choosing one cell to divide and then setting the new cell onto a neighbor site on the lattice, adjacent to the mother cell. In the single-cell-based model a lattice site can be occupied by at most one cell. The offspring is placed randomly on the free neighboring sites. Here different choices are possible. If one considers a choice of position which promises the best environment for the cell, for instance, maximum nutrients or maximum free volume, then the rules may have to be changed. In the case where there is no free neighboring site, cells are pushed away along the shortest track to the nearest free site so that a free adjacent place for the offspring occurs.

By experimental observations of many tumor cell lines Brú *et al.* [16] found a kinetic behavior that shows an exponential growth in the early phase of the development of the cell diameter that then changes to linear growth, so correspondingly a proliferating rim has to be included in the model. This is done by permitting division if there is at least one free lattice site in distance smaller than ΔL from the proliferating cell. In Fig. 1(a) we see the steps for the 2D case with the basic square lattice (white lines), the distributed points (black points), and the Delaunay triangulation (red lines). The shape for a cell, which is chosen to perform an action, is identified here by the dual graph to the triangulation (see the white polygon). The radius of the circle (green) is given by the proliferation length ΔL. If there exists a free lattice site inside this circle, the cell division is possible. In doing so it pushes the neighbors along the shortest track to the free lattice site away, placing the offspring directly next to it. Figure 1(b) shows the considered cell (red) and the adjacent cells inside the proliferation length (blue) on the dual Voronoi lattice in three dimensions. We refer to ΔL as proliferation length. Its values are given in units of lattice constant a. The experimental growth velocities do not agree with a proliferating rim $\Delta L=1$. Thus, $\Delta L>1$ is needed.

For tumor cell populations in general, processes related to migration play a crucial role. If a mutation causes a cell to

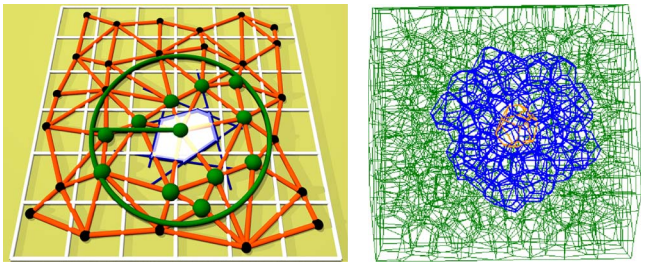

FIG. 1. (Color online) (a) 2D lattice: based on a square lattice (white lines) the Voronoi points (black) are distributed and connected by the Delaunay triangulation (red lines). The corresponding polygon (blue) for the shape of one cell (white) is shown. The radius of the green circle denotes the proliferation length ΔL up to which a dividing cell (white) can proliferate. (b) The dual graph of the analog 3D lattice: the polyhedrons correspond to the cells. Here cells inside the range ΔL of a proliferating cell (orange) are colored blue instead of drawing a sphere surrounding them.

lose its ability to adhere to other cells, it may invade the surrounding tissue [12]. Migration can then cause these cells to invade other parts of the human body and form new tumors. Although it is not our aim to model the metastatic processes of invasive cells in this paper, we consider cell migration.

In our models a cell moves with rate ϕ to an unoccupied neighboring site, irrespectively of the number of neighboring cells before and after its move. This rule corresponds to the case of no cell-cell adhesion. Summarizing our investigations we have to deal with three parameters: the proliferation length ΔL, the migration rate ϕ, and the Erlang number m. The lattice constant a can be absorbed in the space variable and the average cell-cycle time $\bar{\tau}$ in the time variable.

So far, we have defined our underlying structure, namely, the Delaunay triangulation, and we have described the possible processes and parameters in the model. We are now going to outline our method of observing cell population growth. We here use the kinetic Monte Carlo method and we now describe the specific conditions for our simulation.

Kinetic Monte Carlo methods are a well-established tool in simulations for very different types of stochastic growth processes ranging from crystal growth (see, e.g., [34–41]) to investigations of stock market development [42].

The kinetic Monte Carlo method or event-based Monte Carlo makes use of all possible events in the system at time t [43–45]. According to the specific probability of the event, we then step by step choose an event to occur and increase the time by the time step

$$\Delta t = -\frac{1}{r_t}\ln(1-\xi). \tag{2}$$

Here, ξ is a random number uniformly distributed in $[0,1)$, and $r_t=\Sigma_i p_i$ is the sum of all transition rates p_i of possible events which may occur at time t.

We want to explain the development of the cell population and the critical surface dynamics, so our main quantities are the cell diameter of the population and the border cells.

It is obviously important to have a measurement of the size of the cell population which is independent of the morphology. Although we can also analyze growth kinetics using the cell population size $N(t)$, in this case we take the gyration radius defined by

$$R_{gyr} = \sqrt{\frac{1}{N}\sum_{i=1}^{N}(\underline{r}_i - \underline{R}_0)^2}. \tag{3}$$

Here $\underline{R}_0=\frac{1}{N}\Sigma_{i=1}^{N}\underline{r}_i$ is the position of the center of mass. For a compact circular cell aggregate (in $d=2$ dimensions), R_{gyr} is related to the mean radius $\bar{R}(t)=\frac{1}{2\pi}\int_0^{2\pi}R(\varphi,t)d\varphi$ (polar angle φ) of the aggregate by $\bar{R}=R_{gyr}\sqrt{2}$.

B. Three-dimensional model

Brú *et al.* [15–18] analyzed both cell lines of *in vitro* monolayers and cell lines of tumors *in vivo*. In both cases they found strong evidence for the same growth dynamics, and concluded that the growth is based on the same rules. Therefore, to model real systems in three dimensions, it is straightforward to use the same basic rules as in the 2D case. We then are able to compare the results in both cases.

Since all the model rules explained in the previous paragraph can directly be extended to an additional dimension, we just point out the differences:

(a) For the construction of the Delaunay mesh we use a cubic lattice, resulting in an average cell volume of $\bar{V}=a^3$. Each cell has an average of 12 neighbors.

(b) The computation time grows with ΔL^6 in three dimensions instead of ΔL^4 in two. This limits the range of parameters being investigated dramatically.

(c) The connection between radius of gyration R_{gyr} and mean radius $\bar{R}$ of a hard sphere in generalized dimension d is given by $\bar{R}=R_{gyr}\sqrt{(d+2)/d}$ (for $d=3$ one obtains $\bar{R}=R_{gyr}\sqrt{\frac{5}{3}}$).

In vivo 3D tumors grow up to 10^{10} cells. That population size cannot be reached with single-cell models. To overcome this problem we introduce a coarse-grained cell model, which allows for lattice site occupation numbers larger than 1, i.e., $n_{occ}\in\{0,1,\ldots,n_{\max}\}$. Although a coarse-grained cell can be identified with an ensemble of maximum $n_{\max}$ single cells, the cell-cycle states are reduced to only one variable, an average Erlang number m. The model rules basically remain unchanged, except that lattice sites are considered as free for proliferation and migration if $n_{occ}<n_{\max}$:

(a) A cell is able to divide if there is a lattice site with $n<n_{\max}$ in range of ΔL. The offspring is placed on the nearest site for which $n<n_{\max}$ holds.

(b) A cell can migrate if there is a direct neighbor site with $n<n_{\max}$.

We assume that an occupation number greater than 1 corresponds to a space renormalization $\mathbf{x}'=s\mathbf{x}$, with $s=n_{\max}^{1/3}$. Consequently the parameters such as proliferation length ΔL and migration rate ϕ have to be renormalized as well.

To sum up, we have introduced two models to simulate the growth of cell colonies in three dimensions: an individual-cell model, which is used for comparison with the previous 2D simulations, and a nonindividual coarse-grained

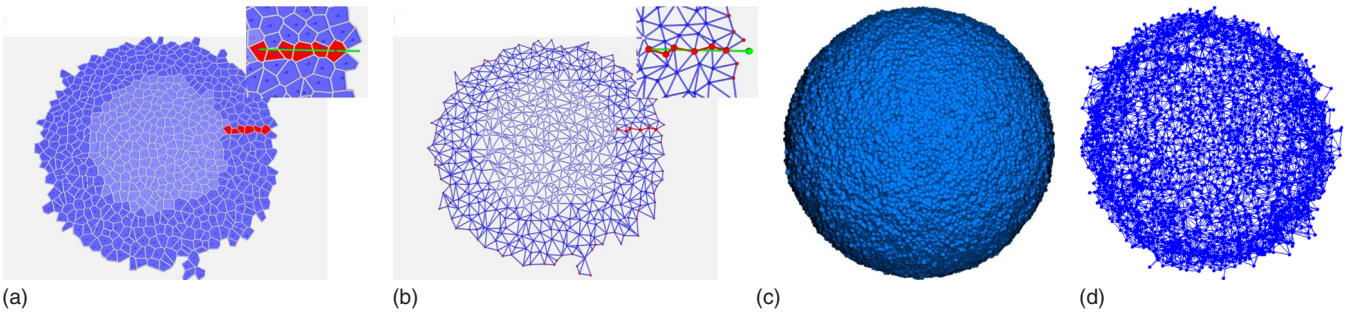

FIG. 2. (Color online) Examples of the irregular lattice and corresponding cell structure in two and three dimensions. (a) The Voronoi structure, i.e., the cell geometry, in the 2D model: inactive cells (light blue) and proliferating cells (dark blue), with an example path for a cell to proliferate inside this rim (light green line), and the involved cells (dark red). (b) The Delaunay lattice structure corresponding to (a): inactive points (light blue), proliferating points (dark blue), path for proliferation (light green line), and involved lattice points (dark red). (c) The Voronoi structure and the cell structure in the 3D model. Cells are depicted as spheres. (d) The Delaunay lattice structure corresponding to (c).

model for comparison with real experiments. With an algorithm based on the first model we are able to perform simulations with up to 10^7 cells on a common personal computer. The second enables us to deal with 10^9 cells or more. In the coarse-grained model the maximum occupation number $n_{\max}$ has to be specified in addition to the parameters of the 2D model $(\Delta L, \phi, m)$.

III. COMPARISON OF THE 2D AND 3D SIMULATIONS

In this section we compare the coarse-grained 3D model with the 2D model and show by comparison that both exhibit the same properties. We first compare the 2D model with the 3D model with $n_{\max}=1$, and discuss the case $n_{\max}>1$ subsequently.

Figure 2 shows how both are constructed. In Figs. 2(a) and 2(b) we see the 2D cases for the dual graphs, the Voronoi structure and the corresponding Delauney triangulation. To emphasize again the general algorithm, in the inset we show for both cases an example of proliferating rim of thickness ΔL (dark blue rim and one example of a cell division in red). In Figs. 2(c) and 2(d) corresponding structures in three dimensions are depicted.

A. Lattice artifacts

An important feature of both models is the avoidance of lattice artifacts in the simulation results. For the 2D model it was shown in detail that for three regular lattice types, namely, the simple square lattice (*von Neumann neighborhood*), the hexagonal lattice, and the octagonal lattice (*Moore neighborhood*), simulations with noise reduction show the underlying lattice structure as an artifact, but that this is not the case for our Voronoi construction [14].

In Fig. 3 we show that also for the 3D model noise reduction by sharpening the cell-cycle distribution or increasing the parameter m of the Erlang distribution is possible. For the 2D square lattice [Fig. 3(a)] and the corresponding 3D cubic lattice [Fig. 3(c)] the underlying structure of the regular lattice shows up as an artifact. If we adopt exactly the same parameters for the irregular Voronoi construction, we obtain the expected round shape [Figs. 3(b) and 3(d)]. Thus we have

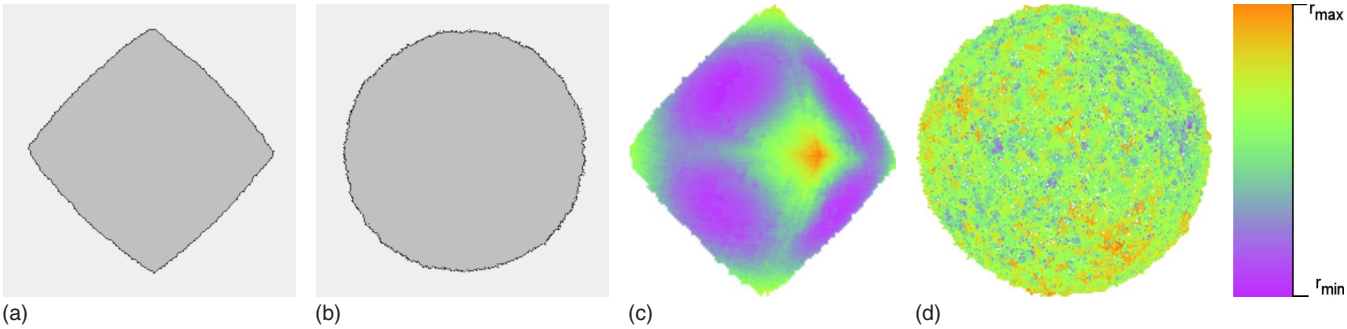

FIG. 3. (Color online) Lattice artifacts in two and three dimensions. (a) Simulation with the individual-cell 2D model on a simple square lattice with $\Delta L=1$, $m=10\,000$, and $\phi=0$. (b) Simulation with the individual-cell 2D model on the Voronoi structure with the same parameters as (a). (c) Simulation with the individual-cell 3D model on a simple cubic lattice with $\Delta L=1$, $m=10\,000$, and $\phi=0$, $n_{\max}=1$. (d) Simulation with the individual-cell 3D model on the Voronoi structure with the same parameters as (c). The color represents the distance from the center of mass in the range between overall minimum and maximum distance. The lattice artifacts in lattice models on regular lattices become the more pronounced the larger m is. With $m\to 1$ (assumption of Poissonian cycle time distribution), increasing ΔL (thick proliferating rim) or if free migration of cells on the lattice (detaching cells that move freely) is considered, the lattice artifacts disappear.

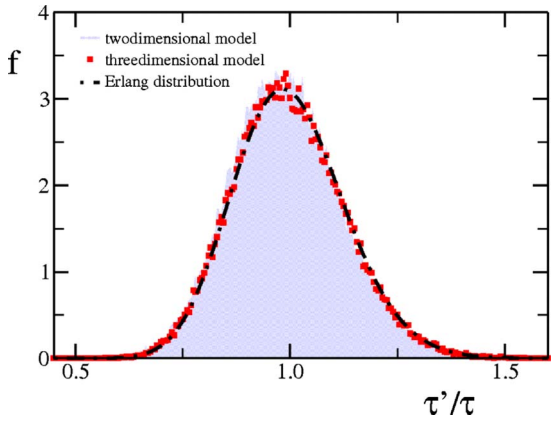

FIG. 4. (Color online) Cell-cycle time distribution of clusters in two (light blue shading) and three dimensions (coarse-grained model; red squares) in comparison with the Erlang distribution (black dash-dotted line). Parameters: $\Delta L=9$, $m=60$, and $\phi=0$ for the 2D model, and $\Delta L=2.21$ with a coarse-grained factor $s=3$ in the 3D model with compounded cells; hence $n_{\max}=27$.

illustrated that both for 2D and 3D our models are free from lattice artifacts.

B. Cell-cycle time distribution

The next step is to show that our models give the same cell-cycle distribution, namely, the Erlang distribution. In Fig. 4 the distribution resulting from our simulations in two and three dimensions together with the theoretical prediction of Eq. (1) is depicted for a fixed set of parameters. They are in very good agreement.

C. Growth kinetics

We continue by investigating the growth kinetics in two and three dimensions, i.e., the time evolution of the gyration radius $R_{gyr}(t)$ of the single-cell-based model. It is qualitatively the same in two and three dimensions and is composed of three growth phases sketched in Fig. 5 for 3D case (for 2D case see Fig. 2a of Ref. [14]). Given an initial radius smaller than the proliferation length, in the beginning a diffusion-like growth (phase I) is observed with $R_{gyr}\propto t^{1/2}$ if the migration rate $\phi>0$, followed by an exponential (phase II). The crossover time between phase I and phase II increases with ϕ; for $\phi=0$, i.e., in the absence of free cell migration, phase I is missed out. In the asymptotic limit the growth becomes linear with constant expansion velocity v_{gyr} (phase III). If ϕ is very large and ΔL is small, then phase II is very short or missed out.

The exponential phase crossing over to linear growth seems to be a robust feature for a wide range of tumor models (see [46,47] and references therein) and is confirmed by several experiments with different cell lines (e.g., [48,49]).

We further analyze the dependence of the expansion velocity v on the Erlang number m, leaving the average cell-cycle time constant. With growing m the cell-cycle distribution peak sharpens and becomes a δ function for $m\to\infty$.

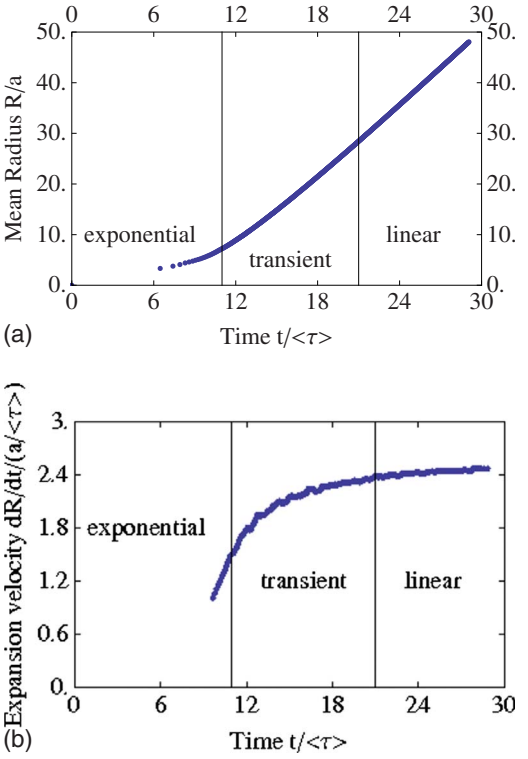

FIG. 5. (Color online) Scheme of the development of the mean radius and the corresponding growth velocity from a 3D simulation with parameters $\Delta L=4$, $\phi=2$, and $m=5$. (a) Radius $\bar{R}$ vs time t divided into three phases of development: an exponential phase, a linear phase, and a transient in between. (b) Growth velocity $v=d\bar{R}/dt$ vs time t averaged over 20 neighboring data points to suppress large fluctuations. The initial $t^{1/2}$ phase is very short due to ϕ being very small; hence it cannot be seen.

Here again we compare the 2D and 3D models (see Fig. 6). For noise-reduced systems ($m>20$) we observe just a weak dependence on the Erlang number. In this case the effective cell-cycle time can be set to $\tau_{\text{eff}}\approx\bar{\tau}/\ln(2)$. The results in both dimensions are in good agreement.

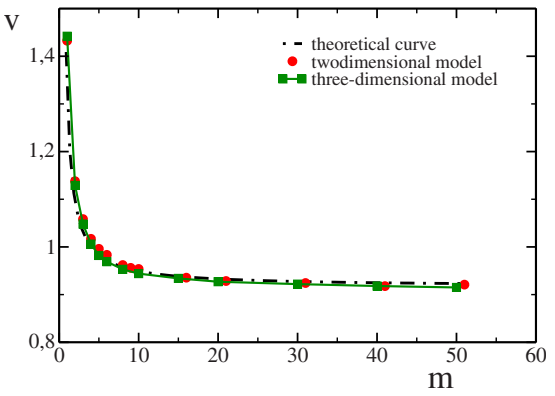

FIG. 6. (Color online) Asymptotic expansion velocity v vs Erlang number m ($\Delta L=1$, $\phi=0$) in two (red) and three (green) dimensions, obtained by single-cell-based kinetic Monte Carlo simulations. The lines are fits using Eq. (4).

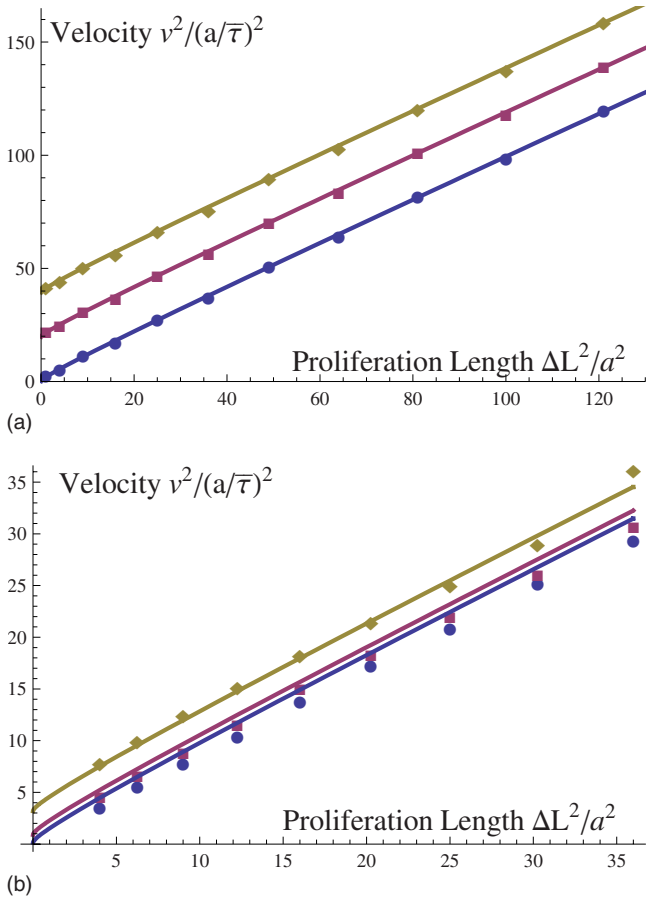

FIG. 7. (Color online) Square of the asymptotic expansion velocity v^2 of the single-cell-based kinetic Monte Carlo simulations vs square of proliferation length ΔL^2. (a) The migration rate is kept constant with values $\phi=0$ (circles), $\phi=10$ (squares), and $\phi=20$ (diamonds) in two dimensions. (b) In three dimensions the migration rate is chosen to be $\phi=0$ (circles), $\phi=0.5$ (squares), and $\phi=2$ (diamonds). In both cases the Erlang number is set to $m=1$. The continuous curves (same color) depict the result of Eq. (4) for the corresponding parameters.

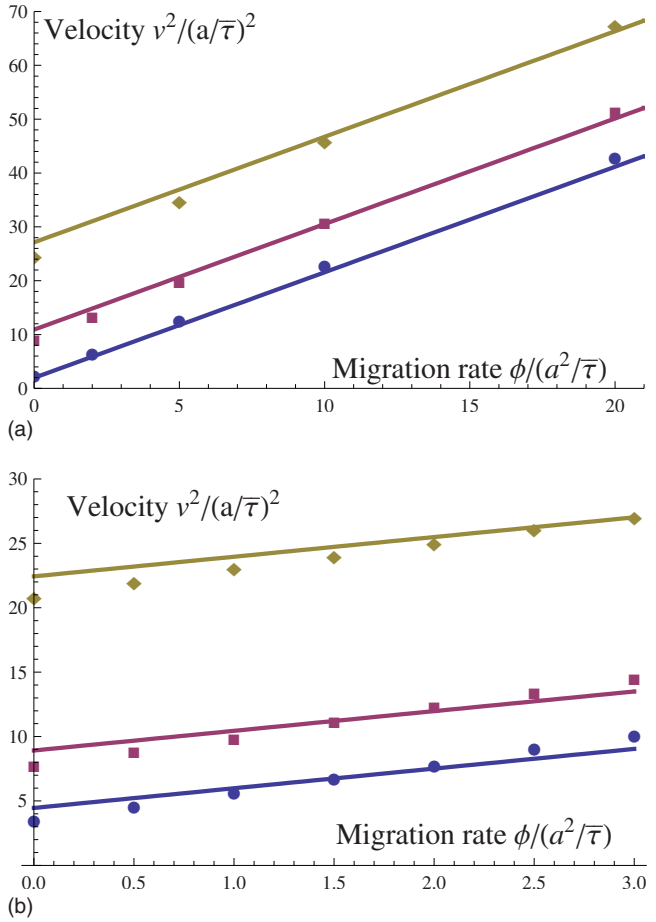

FIG. 8. (Color online) Square of the asymptotic expansion velocity v^2 of the single-cell-based kinetic Monte Carlo simulations vs migration rate ϕ. (a) The proliferation length is kept constant with values $\Delta L=1$ (circles), $\Delta L=3$ (squares), and $\Delta L=6$ (diamonds) in two dimensions. (b) In three dimensions the proliferation length is chosen to be $\Delta L=2$ (circles), $\Delta L=3$ (squares), and $\Delta L=5$ (diamonds). In both cases the Erlang number is set to $m=1$. The continuous curves (same color) depict the result of Eq. (4) for the corresponding parameters.

We find that the time evolution depends on the dimension of the system, while the asymptotic expansion velocity does not. For $v=\frac{d\bar{R}}{dt}\propto v_{gyr}$ we obtain the empirical relation [14], independently of the spatial dimension,

$$v^2 \approx \{B^2[\Delta L'(\Delta L)]^2/\tau_{\text{eff}}^2 + \phi/\tau_{\text{eff}}\}, \tag{4}$$

$$\tau_{\text{eff}}^{-1} = m(2^{1/m}-1)\bar{\tau}^{-1}, \tag{5}$$

$$\Delta L'(\Delta L) = A(\Delta L - 1) + 1, \tag{6}$$

for $d=2,3$. The constants in Eqs. (4)–(6) were obtained by fitting the numerical results (Figs. 7 and 8) found for the expansion velocity and give $A=0.68$ and $B=1.4$ for 2D case [50] and $A=0.708$ and $B=1.236$ for 3D case. Since the numerical data fit quite well to Eqs. (4)–(6) and the constants A and B are approximately the same in both dimensions, we conclude that this is the case for the asymptotic expansion velocity, too. Due to the much larger computational effort, the results in three dimensions fit less accurately than those in two dimensions. The origin of the deviation between $\Delta L'$ and ΔL is a permutation effect: Assuming a δ-like cell-cycle distribution and $\Delta L>1$, the number of proliferating cells in the rim depends on the sequence in which they are chosen. If the cells nearest to the border are chosen first, they block the division of the innermost cells in the rim. Consequently the expansion is slowed down and this is expressed by the factor of 0.68 in Eq. (6). As the cell-cycle distribution smooths, this effect vanishes, which is incorporated by the factor B/τ_{eff}, since $B/\tau_{\text{eff}}(m=1)\approx 1/0.68$.

In the coarse-grained case the effect described above does not occur and Eqs. (4)–(6) are not valid any more. Instead we find for the asymptotic expansion velocity with $\phi=0$

$$v_{\text{coarse}} = s\Delta L_{\text{rescale}}/\bar{\tau}, \tag{7}$$

with $\Delta L_{\text{rescale}}=\Delta L/s$ independently of m ($s=n_{\max}^{1/3}$ as defined in Sec. II B). This is a consequence of the neglect of the individual cell-cycle state information n_{occ}^{k}. Nevertheless, in the case of $m=1$ the situation in our coarse-grained model corresponds to a model where the individual cycle state information is stored in a histogram, since this histogram collapses to a single value. For this reason we will take $m=1$ for comparison with experiments.

The investigated parameter range in these figures differs in two and three dimensions, since, as already mentioned, computation times differ significantly and become exceedingly high in three dimensions.

IV. ANALYTICAL APPROACH TO GROWTH KINETICS

In Sec. III it was shown that the radial growth of the cell colony can be divided into three consecutive regimes. Assuming the system to be in one of these regimes, an analytical description of the time evolution of the mean radius $\bar{R}$ is quite simple and intuitive. In the exponential phase we obtain $\bar{R}(t)\approx C_1 e^{t/(\tau_{\text{eff}}d)}$, and in the linear regime $\bar{R}(t)\approx vt+C_2$. In [46] an approach was suggested which connects phases II and III via a steplike function (e.g., the Hill function) to obtain an overall description of the time evolution. Phase I is not of macroscopic relevance if the migration rate is sufficiently small, which is admissible for many systems.

These phases are, of course, approximations and do not provide any information about the evolution in the crossover regimes in between. In the following we present a very simple analytical model to describe the time evolution of the mean radius that connects these phases and gives a more complicated but accurate approximation.

For $\phi=0$ we assume the cell colony to form a hard sphere of cell number N, which in this case can be connected to the radius via $N=K_d R^d$ with $K_2=\pi/a^2$ and $K_3=4\pi/(3a^3)$ in two and three dimensions. Figure 9 supports this approximation, where the morphologies of the cell colony at different stages of evolution are depicted.

We now take into account that only cells N_P in the proliferating rim of effective thickness ΔL_{eff} at the border of the colony (apparent in Fig. 9) are able to divide, and thus write

$$\frac{dN}{dt}=\frac{N_P}{\tau_m}, \quad \text{with} \quad \tau_m=\begin{cases}\tau_{\text{eff}} & \text{(single-cell model)}\\ \bar{\tau} & \text{(course-grained model)}.\end{cases} \tag{8}$$

For $R\leq\Delta L_{\text{eff}}$ the variable N_P is just the number of cells in the whole colony volume, $N_P=K_d R^d=N$, and for $R>\Delta L_{\text{eff}}$ one gets $N_P=K_d[R^d-(R-\Delta L_{\text{eff}})^d]$. The effective proliferation length $\Delta L_{\text{eff}}=B\Delta L'(\Delta L)$ is given by the numerical results expressed in Eq. (4) for the single-cell case and in the coarse-grained case it is $\Delta L_{\text{eff}}=\Delta L$. Introducing the variable $r:=n^{1/d}$ this leads to the ordinary differential equation

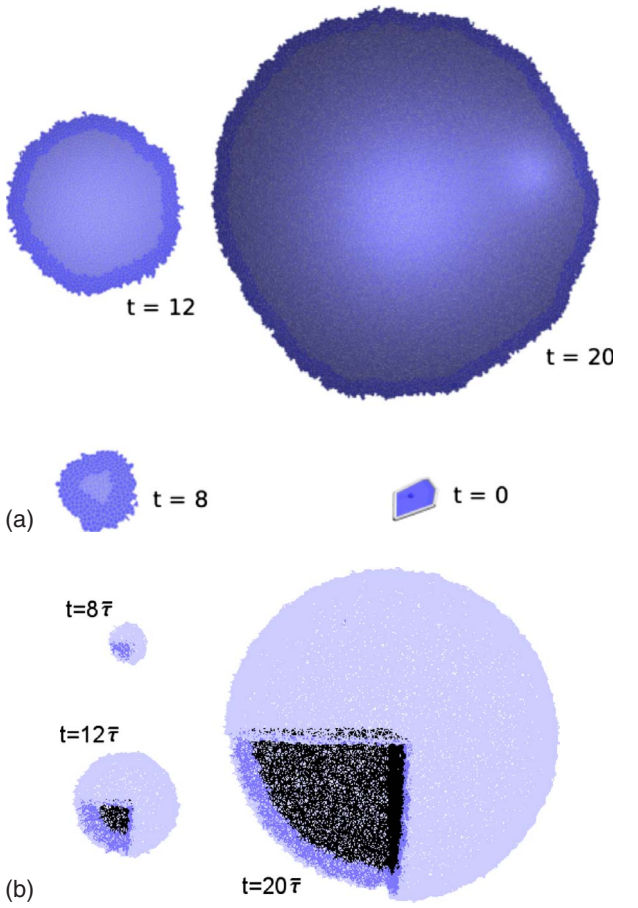

FIG. 9. (Color online) Time evolution of cell colonies with parameters $\Delta L=6$, $\phi=0$, and $m=1$ (single-cell-based model). The colonies are depicted for times $t=8,12,20$ (in units of average cell-cycle time). The active proliferation rim is labeled by color. (a) 2D case: proliferating cells in dark blue and inactive cells in light blue. (b) 3D case: surface cells in light blue, proliferating cells in medium blue, and inactive cells in black. Here one-eighth of the spheroid is cut off, so that the interior becomes visible.

$$\frac{dr}{dt}=\frac{1}{d\tau_m r^{d-1}}[r^d-H(r-K_d^{1/d}\Delta L_{\text{eff}})(r-K_d^{1/d}\Delta L_{\text{eff}})^d], \tag{9}$$

with H being the unit step function. This equation neglects synchronization effects but is still a valuable approximation for sufficiently small Erlang numbers.

Starting at time $t=0$ with $N(0)=N_0$ cells and $R(0)<\Delta L_{\text{eff}}$, the solution in two dimensions is given by

$$r(t)=\begin{cases}\sqrt{N_0}e^{t/(2\tau_m)} & \text{for } t\leq\tau_c\\ \dfrac{\sqrt{K_2}\Delta L_{\text{eff}}}{2}\left[1+W\left(\dfrac{N_0^2}{K_2^2\Delta L_{\text{eff}}^4}e^{1+2t/\tau_m}\right)\right] & \text{for } t>\tau_c,\end{cases} \tag{10}$$

with $W(z)$ being the Lambert function and $\tau_c=\tau_m\ln(\frac{K_2\Delta L_{\text{eff}}}{N_0})$.

In three dimensions the solution has a more complicated form and is given implicitly by

$$\frac{t}{\tau_m} = \begin{cases} \ln(r^3/N_0) & \text{for } r \le r_c \\ \frac{1}{\sqrt{3}}\arctan[p(r)] + \frac{1}{2}\ln[q(r)] + \frac{r}{K_3^{1/3}\Delta L_{\text{eff}}} - \frac{\sqrt{3}}{9}\pi - 1 & \text{for } r > r_c, \text{ with } r_c = K_3^{1/3}\Delta L_{\text{eff}}, \end{cases} \tag{11}$$

with polynomials p and q of r:

$$p(r) = \sqrt{3}\left(\frac{2r}{K_3^{1/3}\Delta L_{\text{eff}}} - 1\right),$$

$$q(r) = \frac{K_3^{4/3}\Delta L_{\text{eff}}^4}{N_0^2}(K_3^{2/3}\Delta L_{\text{eff}}^2 - 3K_3^{1/3}\Delta L_{\text{eff}} r + 3r^2). \tag{12}$$

It can easily be seen that in the limit $r \to \infty$ the asymptotic expansion velocity $v = \frac{dR}{dt}|_{R\to\infty} = K_d^{-1/d}\frac{dr}{dt}|_{r\to\infty}$ that follows from Eqs. (10) and (11) agrees with the findings obtained above, namely, that $v = \Delta L_{\text{eff}}/\tau_m$. Figure 10 shows that the absolute growth kinetics differs in two and three dimensions, while the asymptotic expansion velocity v remains constant. For $d=3$ the colony remains longer in the exponential phase than for $d=2$ since the cells spread in an additional dimension, taking more time to reach a radius of the size of the proliferation length.

In Ref. [46] a different analytical expression for the colony radius was proposed that mimics the transient from the initial exponential to the linear-growth phase using a Hill function $H(t) = t_c^n/(t_c^n + t^n)$ as a "switch." It turns out that analytical expression is not able to capture the transient behavior of our cellular automaton simulations properly for any choice of t_c or n. Figure 10 shows the expression for $t_c = \ln(K_d \Delta L_{\text{eff}}^d/N_0)\tau_m$. For small $n < 10$ the Hill function is not decaying fast enough so that the exponential-growth term remains dominating within the physiological relevant time range. For large $n \ge 10$ the crossover is too sharp. The analytical expression in this paper shows perfect quantitative agreement with the growth kinetics of the cellular automaton models over the whole time range.

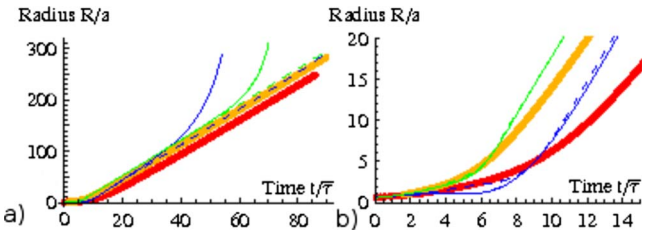

FIG. 10. (Color online) Comparison of the analytical models for the growth kinetics in two and three dimensions. The parameters were chosen to be $\Delta L_{\text{eff}}=5$, $\phi=0$, and $N_0=1$. (a) Long-time development and (b) crossover between exponential and linear regimes. Thick orange (gray) line: result of Eq. (10) ($d=2$); thick red (black) line: result of Eq. (11) ($d=3$). The thin lines are results of the phenomenological growth law presented in [46] using the Hill function $H(t)=t_c^n/(t_c^n+t^n)$—thin green (gray) line: $d=2$, $n=8$; dashed green line: $d=2$, $n=16$; thin blue (black) line: $d=3$, $n=4$; dashed blue line: $d=3$, $n=8$.

Particularly in three dimensions the convergence to the linear asymptotic regime is slow. Thus, the expansion velocities v obtained from experimental or numerical data at a certain radius R may differ from the asymptotes. With an initial guess for the proliferation length, one can use Eq. (9) to determine the relation

$$\frac{v(R)}{v_{asy}} = 1 - \frac{\Delta L_{\text{eff}}}{3R^2}(3R - \Delta L_{\text{eff}}). \tag{13}$$

Recalculating ΔL and using this equation again gives an iterative procedure, but taking the first order is sufficient in most cases.

V. VALIDATION BY COMPARISON TO EXPERIMENTS

In Ref. [14] it was shown that the presented lattice-based cellular automaton model in two dimensions is able to reproduce the experimental results concerning the growth kinetics found in Refs. [15,16] of rat astrocyte glioma monolayers *in vitro*. As we will see in Sec. VI, it does not make sense to compare the three-dimensional numerical data to experimental results of monolayer (2D) cell aggregates. Thus we compare 2D and 3D cases separately. In order to compare the numerical results with experiments in three dimensions we construct a coarse-grained model that can deal with sufficiently high cell numbers of about 10^9 cells, which appear in common cell colonies. The results of this model are analogous to the single-cell-based model in three dimensions; i.e., choosing the correct rescaled parameters will give approximately the same kinetics.

To obtain the set of parameters for reproducing experimental data, the asymptotic expansion velocity is measured and the iterative correction based on Eq. (13) is used. The result gives ΔL using Eq. (7). The monolayers form a one-cell-thick dense cell aggregate [15], the xenografts a solid approximately spheroidal dense aggregate so free migration of cells can be neglected; hence $\phi=0$. Since in the coarse-grained model v_{coarse} is independent of m, we choose $m=1$ for the reason described in Sec. III C and to save computation time. Note that the effect of choosing $m=1$ instead of $m \approx 5-60$ is a speedup in the growth velocity by a factor of ≈ 1.4 as we have shown in Fig. 6 and, as we will show in Sec. VI, transient oscillations for small cell population sizes. However, in the experimental data, oscillations could not be found, suggesting that for the experimentally observed range of population sizes, synchronization effects could be neglected. In Sec. VI we will show that for $m=5-100$ such oscillations are expected to disappear at population sizes of $N \approx 10^3$ cells, corresponding to cell aggregate radii of about 200–300 μm in two dimensions and 150 μm in three dimensions, which justifies our assumption of $m=1$.

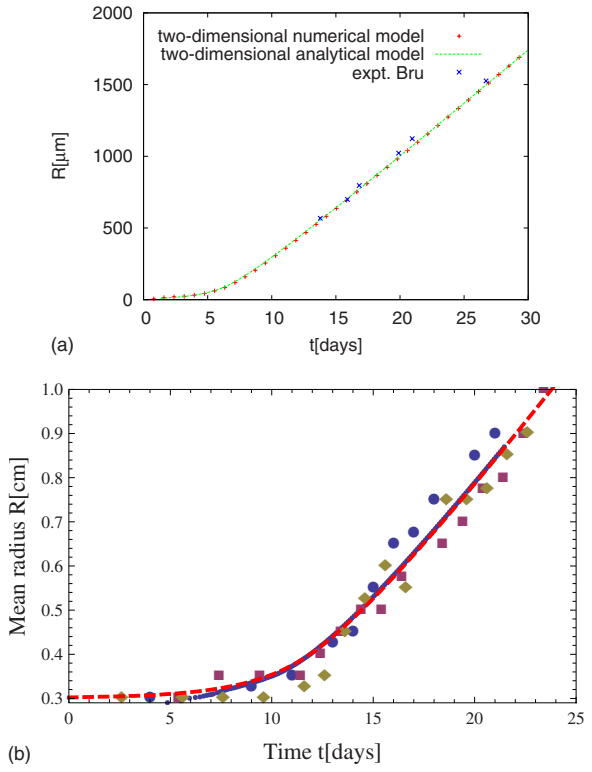

FIG. 11. (Color online) Mean radius R of the cell aggregate vs time t. (a) In two dimensions—blue crosses: experiment for C6 rat astrocyte glioma cells [15,16]; red pluses: kinetic Monte Carlo simulation of the 2D model with the same parameters as in Fig. 4; green line: analytical result of Eq. (10) with $\Delta L_{\text{eff}}=BL'\approx 8.725$ and $N_0=1$, corresponding approximately to $\Delta L=9$. We chose $l=10$ μm for the cell diameter and $\tau=19$ h for the cell-cycle duration as in Ref. [14]. (b) Three dimensions—blue circles, green diamonds, violet squares: *in vivo* NIH3T3 mouse-fibroblast xenografts; solid blue line: coarse-grained kinetic Monte Carlo simulations with parameters $\Delta L=2.85$, $\phi=0$, $m=1$, and $n_{\max}=1000$; dashed red line: analytical result of Eq. (10) with $\Delta L_{\text{eff}}=28.5$ and $N_0=1$. We have chosen $l=17$ μm [51] and $\tau=24$ h [52].

Figure 11(a) compares the experimental data for the growth kinetics of a tumor cell line (rat astrocytes [16]) with the 2D numerical and analytical model of Secs. II–IV. In these monolayer cultures, all cells have access to nutrients; hence limiting effects of nutrients on the growth kinetics do not occur. From the comparison of experimental and simulation results, we conclude that the crossover from an initial exponential- to a linear-growth phase seems to emerge from contact inhibition of cell division. In Fig. 11(b) we compare both our computer simulations and our coarse-grained model with experimental findings for a tumor growing subcutaneously in mice [53] to be able to compare the data obtained *in vitro* [Fig. 11(a)] to the *in vivo* situation. For this purpose we used NIH3T3 cells transformed by expression of the human oncogene erbB2. After injection into nude mice these cells form subcutaneously proliferating tumors [53]. The three-dimensional growth of the resulting tumors could be modeled using the coarse-grained cellular automaton model. The xenografts are well vascularized and only sporadically small necrotic lesions are found, so that we assume oxygen and glucose are not the major factors limiting tumor growth. Instead, contact inhibition seems to control the speed of expansion as proposed in Refs. [46,54] for multicellular spheroids growing in liquid suspension.

VI. SYNCHRONIZATION EFFECTS

In this section we want to describe the influence of synchronization on the growth kinetics of a cell colony. As explained above, in our work the cell-cycle time distribution is mimicked by an Erlang distribution, parametrized by the Erlang number m. High Erlang numbers m lead to a sharp distribution of cell-cycle times. As a consequence cells are more likely to perform division at the same time. This synchronization results in oscillations of the variables $\bar{R}(t)$ and $N(t)$ describing the growth kinetics. In this part of our paper we focus on the question of how synchrony of the cell population decreases with time and how this depends on the Erlang number. Knowing until which cell population size oscillations should be visible in the data depending on the Erlang number m may permit estimation of the Erlang parameter m and thereby the cell-cycle time dispersion directly from experimental data on the growth kinetics of cell population sizes without extra experiments using cell proliferation markers. For example, in the experiments discussed in Sec. V the experimental data did not show oscillations, suggesting that within the observed range of radii no synchronization effects were present. For synchronized cell populations either by drugs or by a circadian clock, the expected situation could be very different.

In the presented cellular automaton model the Erlang distribution of the cell-cycle times with number m is generated by letting a cell pass through m states $q_1,q_2,\ldots,q_m$ with equal transition rate θ between q_k and q_{k+1}. If a cell in state q_m is chosen, it divides and two offsprings are generated on the lattice, each being in the same state q_1. At the time of their creation these cells are synchronized. Due to the statistical behavior of the system they desynchronize. Notice that the different intermediate values q_i, with $i\in[1,m]$, of the Erlang distribution do not necessarily represent true intermediate states of the cell cycle. We rather used this description because the emerging cell-cycle distribution resembles those found in experiments [33].

Now it is an important issue how synchronization is defined. There exist different definitions (see, e.g., [55]). One possibility is to define such a measure as the deviation of the state distribution [i.e., the possibility $p(q_k)$ of a cell to be in state q_k] from the equidistribution. Instead we use a measure of synchrony which can easily be obtained by experiments: the amplitude of the oscillatory offset.

From Sec. V we know that the population size in the exponential phase is given by $N_{\text{appr}}(t)\approx N_0 e^{t/\tau_{\text{eff}}}$. For high Erlang number m this approximation fails and we obtain

$$N(t)=N_{\text{appr}}(t)+N_{\text{osci}}(t). \tag{14}$$

In the following we calculate the form of the second term N_{osci} from our model, focusing on the role of the Erlang number. For simplicity we assume that the population stays in the exponential-growth phase, which ensures that the cells

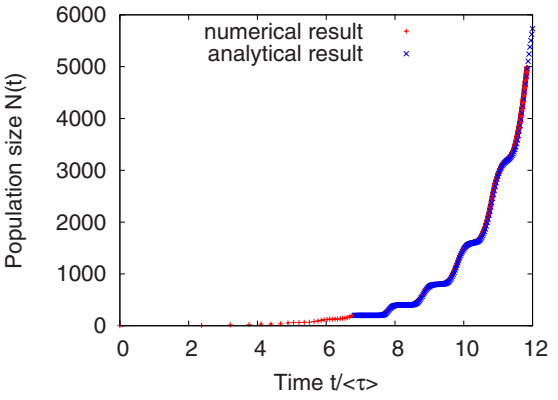

FIG. 12. (Color online) Comparison of numerical simulation and analytical result of the population size $n(t)$ for high Erlang numbers in the exponential-growth phase. Red crosses: individual-cell-based model with $\Delta L=8$, $\phi=0$, and $m=100$. Blue pluses: Analytical result of Eq. (14) for $m=100$. The population was synchronized at time $t\approx 6.3\bar{\tau}$.

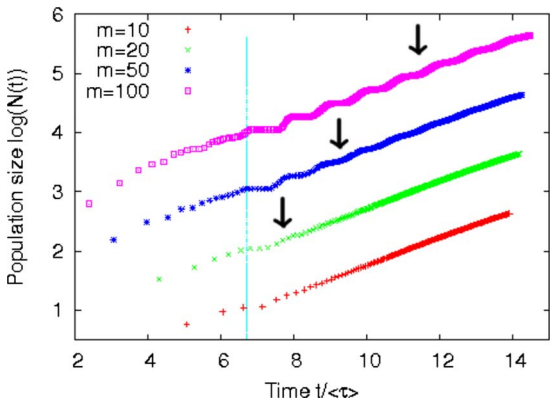

FIG. 13. (Color online) Population sizes vs time for different Erlang numbers $m=10,20,50,100$ in a half-logarithmic diagram. The 3D individual-cell-based model was used with the parameters $\Delta L=8$ and $\phi=0$. The vertical blue line represents the time of total synchronization. An ordinate offset between the curves was added for convenience so as to not let them overlap.

do not stop their cycle. Hence cells once generated on the lattice do not interact according to their proliferative behavior. The only interaction—and this is the mechanism of synchronization in this model—is cell division itself. Without this mechanism the statistical dynamics would cause the system to desynchronize faster.

In this case by considering a large ensemble one can set up a linear dynamic system describing the time evolution of the number of cells n_k being in state q_k. The initial conditions are chosen in a way that the population is totally synchronized in the beginning,

$$\dot{n}_1 = -n_1 + 2n_m, \quad k=1, \tag{15}$$

$$\dot{n}_k = -n_k + n_{k-1}, \quad k=2,\ldots,m, \tag{16}$$

$$n_k(0) = N_0\delta_{k1}, \quad k=1,\ldots,m, \tag{17}$$

$$N = \sum_{k=1}^{m} n_k. \tag{18}$$

This system (the rate is absorbed by $t\mapsto\theta t$) can be solved analytically for arbitrary Erlang number m. The solution has the form of Eq. (14). A comparison of this solution and the 3D numerical model is depicted in Fig. 12 and confirms that the presented equations give a good description in the exponential phase. The first term N_{appr} contains the real eigenvalues and is dominated by $e^{t/\tau_{\text{eff}}}$ corresponding to the highest real eigenvalue; the second belongs to the imaginary eigenvalues. Considering the relative oscillation $\theta := N_{\text{osci}}/N$, we find that $\theta(t)\approx e^{-t/\tau_{\text{eff}}}N_{\text{osci}}(t)$. The lowest frequency

$$\omega_{\min} = \frac{2\pi}{T_{\max}} = 2^{1/m}\sin(2\pi/m) = 2\pi\left(\frac{1}{m}+\frac{\ln 2}{m^2}\right)+O\left(\frac{1}{m^3}\right) \tag{19}$$

belongs to the eigenvalue with the second highest real part dominating the oscillations. We therefore have shown that the amplitude of the relative oscillation decays exponentially and define the *synchronization time* τ_{sync} by the damping factor $e^{-t/\tau_{\text{sync}}}$. Thus we get

$$\tau_{\text{sync}} = \frac{m^2}{2\pi^2}\left(1+\frac{\ln 2}{m}\right)+O\left(\frac{1}{m^0}\right). \tag{20}$$

We now introduce the *synchronization number* $S := \tau_{\text{sync}}/T_{\max}$, which describes how many oscillation periods can be seen until the amplitude drops to the e^{-1}-fold of the initial value, and find

$$S \approx \frac{m}{2\pi^2}, \quad m \gg 1. \tag{21}$$

To confirm this result we performed simulations in three dimensions with different Erlang numbers m, leaving the average cell-cycle time constant. Instead of investigating the effects from the beginning with one initial cell, a population was grown and artificially synchronized at a certain time when the population size was sufficiently high to have a large ensemble. This prevents the data from becoming too noisy. Additionally a high proliferation length was chosen to keep the population in the exponential-growth phase. The results can be seen in Fig. 13. The linear behavior in the half-logarithmic plot makes clear that the population stays in the exponential regime. The relaxation times of the oscillation agree well with the theory and the fact that significant oscillations ($S>1$) are not visible until $m>2\pi^2\approx 20$. Thus in the exponential-growth regime our theoretical considerations are able to explain the synchronization behavior of the simulated cell populations.

VII. CONCLUSION

In this paper, we have presented three different models for cell populations in three dimensions: a single-cell-based model, a coarse-grained model, and an analytical model. The asymptotic expansion velocity v of the cell populations can be related in these three models by the following argument.

Assuming $\phi=0$, the proliferation length in each model has to be chosen in the following ways to obtain the same asymptotic expansion velocity:

(a) single-cell model: $v=B\Delta L'(\Delta L)/\tau_{\mathrm{eff}}$

(b) coarse-grained model: $v=s\Delta L_{\mathrm{rescale}}/\bar{\tau}$

(c) analytical model (coarse/fine): $v=\Delta L_{\mathrm{eff}}/\tau_m$

Equating this leads to

$$\Delta L_{\mathrm{rescale}} = sB\Delta L'(\Delta L)\frac{\bar{\tau}}{\tau_{\mathrm{eff}}}, \tag{22}$$

$$\Delta L_{\mathrm{eff}} = B\Delta L'(\Delta L)\frac{\tau_m}{\tau_{\mathrm{eff}}}. \tag{23}$$

The main goal of this paper is to compare the features of the proposed 3D model for cell population growth with its 2D version. This was done on a Dirichlet lattice in order to avoid lattice artifacts. In both cases the numerical calculations yield the same qualitative behavior: an initial phase obeying a $t^{1/2}$ power law which is missed out if cells cannot detach from the tumor is followed by a transient exponential growth and an asymptotic linear regime in the end. The dependence of the asymptotic expansion velocity on the parameters of proliferation length, migration rate, and Erlang number was examined and we showed that the law found in [14] is valid in three dimensions, too. Nevertheless the 2D model is not appropriate to model the exact time evolution of the mean radius of a 3D cell colony, since in the latter case it stays longer in the exponential phase. We propose a simple analytical approach to include this fact which can give a suitable approximation for the kinetics if the migration rate is zero.

A comparison of the numerical and analytical models to the experimental data in two and three dimensions is given and shows that they approximately agree. The single-cell-based models may be validated by measuring the thickness of the proliferating rim (e.g., by BrdU [56] or Ki67 labeling [53]), the cell-cycle duration (e.g., by cohort experiments [57]), and visualizing detaching cells (*in vitro* by live imaging [58], or light or confocal microscopy; *in vivo* by biopsy followed by image analysis). If growth-inhibited cells are mainly arrested in cell-cycle checkpoints after the restriction point, the measured thickness should correspond to the proliferation length ΔL. However, the relation between growth velocity and the experimentally observed proliferation length should involve an additional proportionality factor that depends on the distribution of cell-cycle checkpoints in which growth-inhibited cells are arrested. Experiments are necessary to identify such possible proportionality factors. The cohort experiments permit determination of the cycle time length distribution and hence $\bar{\tau}$ and m. Apoptosis would rescale our growth rate and can experimentally be detected by TdT-mediated dUTP-biotin nick end labeling (TUNEL) assay [53]. If the tumor is basically compact, i.e., if the thickness of the proliferating rim is large compared to the length scale at which detached cells can be found, the approximation of this paper should directly be applicable. For the coarse-grained model, the parameters can be determined from the parameters of the single-cell-based models as explained above.

Additionally in this paper, we consider the situation when the Erlang number is large, resulting in a sharply peaked cell-cycle distribution. An initially synchronized cell population will then show an oscillatory offset which is damped out in time. We have introduced a synchronization time, i.e., the time the population stays synchronized, which is the reciprocal of the damping factor.

Computations based on our model in three dimensions are much more time consuming than in two dimensions, limiting the range of parameters and cell numbers significantly. The coarse-grained algorithm is an alternative for large population sizes but neglects individual information about the cells. Since the qualitative behavior of the radial kinetics is equal in each of the presented models, we suggest that the single-cell-based model in two dimensions is sufficient to describe the generic features of population growth. Our results confirm that in cases where more precise predictions are of importance, e.g., in medical research, 3D simulations are necessary.

There are several perspectives of continuing the current work. One possibility is to develop more sophisticated coarse-grained models, incorporating, for example, adaptive grid methods. It would then be possible to model regions of interest such as the colony surface with high resolution, while the inner part is represented by coarse-grained cells. In this case if the number of cells at the surface of the colony is high enough, the universality class of the growth could be determined and compared to those in Refs. [14,15].

Further, it would be interesting to validate the predicted behavior of desynchronization by experiments to test if the assumption of Erlang-distributed cell cycles is a good approximation. This could be done, for example, by measuring the mitosis rate of a colony versus time [57]. Due to its simplicity, the proposed model is of generic character and therefore serves as a basis for more complex models. However, a possible next step would be to implement a mechanism which represents a therapy by triggering apoptosis, causing the cell colony (tumor) to shrink.

ACKNOWLEDGMENTS

D.D. acknowledges support by the EU grants CANCERSYS and PASSPORT, and the BMBF grants LungSys, under Grant No. 0315415F, and Hepatosys, under Grant No. 313074D.

[1] J. A. Adam and N. Bellomo, *A Survey of Models for Tumor-Immune System Dynamics* (Birkhäuser, Boston, 1997).

[2] R. A. Gatenby and P. K. Maini, Nature (London) **421**, 321 (2003).

[3] R. P. Araujo and D. L. McElwain, Bull. Math. Biol. **66**, 1039 (2004).

[4] L. Preziosi, *Cancer Modelling and Simulation* (Chapman and Hall, London/CRC, Cleveland, 2003).

[5] T. Roose, S. J. Chapman, and P. K. Maini, SIAM Rev. **49**, 179 (2007).

[6] J. Moreira and A. Deutsch, Adv. Complex Syst. **5**, 247 (2002).

[7] M. S. Alber, M. A. Kiskowski, J. A. Glazier, and Y. Jiang, in *Mathematical Systems Theory in Biology, Communication, and Finance*, Vol. 134, edited by J. Rosenthal and D. S. Gilliam (Springer, New York, 2003), pp. 1–42.

[8] D. Drasdo, in *Multiscale Modeling*, edited by W. Alt, M. Griebel, and J. Lenz (Birkhäuser, Basel, 2003).

[9] J. Galle, G. Aust, G. Schaller, T. Beyer, and D. Drasdo, Cytometry, Part A **69A**, 704 (2006).

[10] A. R. A. Anderson, M. A. J. Chaplain, and K. A. Rejniak, *Single-Cell-Based Models in Biology and Medicine* (Birkhäuser, Basel, 2007).

[11] T. Alarcon, H. M. Byrne, and P. K. Maini, J. Theor. Biol. **229**, 395 (2004).

[12] I. Ramis-Conde, D. Drasdo, A. R. A. Anderson, and M. Chaplain, Biophys. J. **95**, 155 (2008).

[13] I. Ramis-Conde, M. A. Chaplain, A. R. Anderson, and D. Drasdo, Phys. Biol. **6**, 16008 (2009).

[14] M. Block, E. Schöll, and D. Drasdo, Phys. Rev. Lett. **99**, 248101 (2007).

[15] A. Brú, S. Albertos, J. L. Subiza, J. López García-Asenjo, and I. Brú, Biophys. J. **85**, 2948 (2003).

[16] A. Brú, J. M. Pastor, I. Fernaud, I. Brú, S. Melle, and C. Berenguer, Phys. Rev. Lett. **81**, 4008 (1998).

[17] A. Bru, S. Albertos, J. A. Lopez Garcia-Asenjo, and I. Bru, Phys. Rev. Lett. **92**, 238101 (2004).

[18] A. Brú, S. Albertos, J. L. Garcia-Asenjo, and I. Brú, J. Clin. Res. **8**, 9 (2005).

[19] F. Lévi, E. Filipski, I. Iurisci, X. M. Li, and P. Innominato, Cold Spring Harb. Symp. Quant. Biol. **72**, 465 (2007).

[20] D. R. Appleton, P. J. Thomson, C. E. Donaghey, C. S. Potten, and M. McGurk, Cell Prolif **35**, 68 (2002).

[21] J. M. Qiu, S. A. Roberts, and C. S. Potten, Epithelial Cell Biol. **3**, 137 (1994).

[22] R. Baserga, Cancer Res. **25**, 581 (1965).

[23] E. Filipski, F. Delaunay, V. M. King, M. W. Wu, B. Claustrat, A. Grechez-Cassiau, C. Guettier, M. H. Hastings, and F. Levi, Cancer Res. **64**, 7879 (2004).

[24] C. Nicolini, Biochim. Biophys. Acta **458**, 243 (1976).

[25] K. Tomita and J. E. Plager, Cancer Res. **39**, 4407 (1979).

[26] K. P. Hoyer, R. C. Hider, and J. B. Porter, Cancer Res. **52**, 4591 (1992).

[27] J. Breder, S. Rüller, E. Rüller, M. Schlaak, and J. van der Bosch, Exp. Cell Res. **223**, 259 (1996).

[28] M. E. Boon and F. C. Siemens, Acta Cytol. **51**, 73 (2007).

[29] A. Okabe, H. M. J. Boots, K. Sugihara, and S. N. Chiu, *Spatial Tessellations: Concepts and Applications of Voronoi Diagrams, Probability and Statistics*, 2nd ed. (Wiley, New York, 2000).

[30] The precise algorithm we use to construct the Voronoi diagram is depicted in Ref. [29].

[31] D. Drasdo, S. Höhme, and M. Block, J. Stat. Phys. **128**, 287 (2007).

[32] K. Albe, K. Nordlund, J. Nord, and A. Kuronen, Phys. Rev. B **66**, 035205 (2002).

[33] P. Rosen and D. S. Misfeldt, Proc. Natl. Acad. Sci. U.S.A. **77**, 4760 (1980).

[34] A. L. Barabási and H. E. Stanley, *Fractal Concepts in Surface Growth* (Cambridge University Press, Cambridge, England, 1995).

[35] J. Krug, Physica A **313**, 47 (2002).

[36] T. Michely and J. Krug, *Islands, Mounds and Atoms*, 1st ed. (Springer, Berlin, 2004).

[37] M. Meixner, E. Schöll, V. A. Shchukin, and D. Bimberg, Phys. Rev. Lett. **87**, 236101 (2001); **88**, 059901 (2002).

[38] M. Meixner and E. Schöll, Phys. Rev. B **67**, 121202(R) (2003).

[39] M. Meixner, R. Kunert, and E. Schöll, Phys. Rev. B **67**, 195301 (2003).

[40] F. Elsholz, E. Schöll, and A. Rosenfeld, Appl. Phys. Lett. **84**, 4167 (2004).

[41] M. Block, R. Kunert, E. Schöll, T. Boeck, and T. Teubner, New J. Phys. **6**, 166 (2004).

[42] R. N. Mantegna and H. E. Stanley, *Econophysics: An Introduction* (Cambridge University Press, Cambridge, England, 1999).

[43] A. B. Bortz, M. H. Kalos, and J. L. Lebowitz, J. Comput. Phys. **17**, 10 (1975).

[44] D. T. Gillespie, J. Comput. Phys. **22**, 403 (1976).

[45] K. A. Fichthorn and W. H. Weinberg, J. Chem. Phys. **95**, 1090 (1991).

[46] D. Drasdo and S. Höhme, Phys. Biol. **2**, 133 (2005).

[47] S. A. Menchón and C. A. Condat, Phys. Rev. E **78**, 022901 (2008).

[48] J. P. Freyer and R. M. Sutherland, J. Cell Physiol. **124**, 516 (1985).

[49] J. P. Freyer and R. M. Sutherland, Cancer Res. **46**, 3504 (1986).

[50] This value is slightly larger than that given in Ref. [14] and results from a larger number of realizations of growth simulations in both two and three dimensions.

[51] B. Alvarez, E. Garrido, J. A. Garcia-Sanz, and A. C. Carreira, J. Biol. Chem. **278**, 26466 (2003).

[52] A. Degushi, K. Segawa, K. Hosaka, I. B. Weinstein, and K. Umezawa, Jpn. J. Cancer Res. **93**, 157 (2002).

[53] I. B. Schiffer, S. Gebhard, C. K. Heimerdinger, A. Heling, J. Hast, U. Wollscheid, B. Seliger, B. Tanner, S. Gilbert, T. Beckers, S. Baasner, W. Brenner, C. Spangenberg, D. Prawitt, T. Trost, W. G. Schreiber, B. Zabel, M. Thelen, H. A. Lehr, F. Oesch, and J. G. Hengstler, Cancer Res. **63**, 7221 (2003).

[54] J. Galle, M. Loeffler, and D. Drasdo, Biophys. J. **88**, 62 (2005).

[55] A. Pikovsky, M. G. Rosenblum, and J. Kurths, *Synchronization, A Universal Concept in Nonlinear Sciences* (Cambridge University Press, Cambridge, England, 2001).

[56] M. Alison and C. Sarraf, *Understanding Cancer* (Cambridge University Press, Cambridge, England, 1997).

[57] J. A. Smith and L. Martin, Proc. Natl. Acad. Sci. U.S.A. **70**, 1263 (1973).

[58] Y. L. Wang, K. M. Hahn, R. F. Murphy, and A. F. Horwitz, J. Cell Biol. **174**, 481 (2006).